HAL open science

Ab-initio transport simulations unveil the Schottky versus Tunneling barrier trade-off in metal-TMD contacts

D. Lizzit, P. Khakbaz, F. Driussi, Marco Pala, D. Esseni

▶ **To cite this version:**

D. Lizzit, P. Khakbaz, F. Driussi, Marco Pala, D. Esseni. Ab-initio transport simulations unveil the Schottky versus Tunneling barrier trade-off in metal-TMD contacts. 68th IEEE International Electron Devices Meeting (IEDM 2022), Dec 2022, San Francisco, CA, United States. pp.28.2.1-28.2.4, 10.1109/IEDM45625.2022.10019449 . hal-04123805

HAL Id: hal-04123805

https://hal.science/hal-04123805v1

Submitted on 9 Jun 2023

HAL is a multi-disciplinary open access archive for the deposit and dissemination of scientific research documents, whether they are published or not. The documents may come from teaching and research institutions in France or abroad, or from public or private research centers.

L'archive ouverte pluridisciplinaire **HAL**, est destinée au dépôt et à la diffusion de documents scientifiques de niveau recherche, publiés ou non, émanant des établissements d'enseignement et de recherche français ou étrangers, des laboratoires publics ou privés.

Ab–initio transport simulations unveil the Schottky versus Tunneling barrier trade–off in metal–TMD contacts

D. Lizzit[1], P. Khakbaz[1], F. Driussi[1], M. Pala[2], and D. Esseni[1]
[1]DPIA, University of Udine, Via delle Scienze 206, Udine, Italy; [2]Université Paris-Saclay, CNRS, C2N, Palaiseau, France
email: daniel.lizzit@uniud.it.

***Abstract*—We investigate several options for metal contacts to monolayer 2D semiconductors with an in–house developed, *ab–initio* transport methodology. We identify an optimum separation between the metal and the semiconductor resulting in minimum contact resistance ($R_{\rm C}$). Such a minimum $R_{\rm C}$ is fundamentally related to the trade–off between Schottky barrier height and tunneling barrier width. We examine quantitatively the effects of buffer layers and report, for the first time, *ab–initio* $R_{\rm C}$ calculations for the bismuth–MoS_2 system, comprising the influence of the inelastic electron–phonon interaction. Finally, we investigate Au–WSe_2 as a material system for a low $R_{\rm C}$ p–type contact.

I. Introduction

Atomically thin transition metal dichalcogenides (TMDs) have a wide range of applications in many fields [1]–[3], and one of the biggest challenges is to obtain low–$R_{\rm C}$, Ohmic contacts to TMDs, so as to unleash their intrinsic potentials. Even if TMDs have no surface dangling bonds, a large Fermi level pinning (FLP) has been repeatedly reported at metal-TMD interfaces [4], [5]. While the FLP observed in experiments may be partly due to defects [4], even for atomically perfect interfaces the metal-induced-gap-states (MIGS) result in a significant Schottky barrier height (SBH) [6], [7], which degrades the contact resistance and the current drivability.

The insertion of proper buffer layers (e.g. monolayer hBN) between the metal and the TMD has been explored to depin the Fermi level (E_F) in metal–MoS_2 contacts [5], [7]. However the reduction of FLP comes at the cost of a larger tunnelling barrier (TB) in the van der Waals gap (see **Fig.1c**), so that the state–of–the–art resistance for metal–TMD contacts has been stagnating around 1 k$\Omega\,\mu$m for quite many years. Recent experimental results have shown that the semimetallic Bi can effectively suppress MIGS and lead to a low resistance n–type Ohmic contact to several TMDs [8]. Moreover, also Sb [9], [10], and In(Sn)/Au [11] in contact to monolayer MoS_2 have been proposed to decrease $R_{\rm C}$ below the k$\Omega\,\mu$m range.

In this work, we first extend to (semi)metal–TMD vertical heterojunctions (VHJ) our *ab–initio* quantum transport methodology presented in [12], [13]. Then we systematically investigate the influence on the $R_{\rm C}$ of the metal–to–TMD separation and of possible buffer layers inserted in the VHJs.

II. Simulation methodology

Quantum ESPRESSO (QE) was used to investigate within the Density Functional Theory (DFT) some heterostructures with TMDs and (semi)metals [14]. For Al (Au) metal the 111–surface of a six–layer crystal was matched to a $\sqrt{3}\times\sqrt{3}$ MoS_2 (WSe_2) unstrained monolayer supercell (see **Figs.1d** and **2a**), so as to minimize strain, and then relaxation was used to reduce residual forces on atoms [15]. Spurious coupling with periodic replicas of the supercell was minimized by including $\sim$1.5 nm of vacuum along z and by duly employing the dipole correction [14]. For simulations with the semimetallic bismuth (Bi), a 2×2 supercell of three Bi(0001) layers has been matched to a $\sqrt{7}\times\sqrt{7}$ unstrained MoS_2 cell (see **Fig.6**). We employed the Perdew–Burke–Ernzerhof exchange–correlation functional with DFT–D3 van der Waals corrections. After a complete geometry optimization, the extracted distances between metal and TMD are d=0.27, d=0.71, d=0.32 and d=0.28 nm for Al–MoS_2, Al–hBN–MoS_2, Bi–MoS_2 and Au–WSe_2, respectively, in good agreement with [8], [16], [17].

In order to extend the rigour of DFT calculations to transport properties, we modeled the conductance across the heterostructures of **Fig.1a** by employing the *ab–initio* quantum transport methodology based on the Non Equilibrium Green's Functions (NEGF) approach presented in [12]. Our method starts from the plane–wave DFT Hamiltonian obtained from QE, and reduces the size of the Hamiltonian blocks by transforming first to the hybrid basis $x\mathbf{K}_{yz}$, and then to a basis set consisting of unit–cell restricted Bloch functions (URBF) [12]. **Fig.1e** shows how the URBF basis can provide an accurate band reconstruction even in the complex Al–hBN–MoS_2 supercell, and by using $\approx$450 URBFs, instead of the $\approx$72000 plane waves used in QE calculations. Originally conceived for homogeneous systems, the transport method in [12] has been here extended to deal with the heterostructures in **Fig.1a** [13]. To this purpose, first the Hamiltonian blocks $[\mathbf{H}_{00}^{(i)}]_\Phi$, $[\mathbf{H}_{01}^{(i)}]_\Phi$ in the URBF basis were extracted for each sub–system ($i=1,2,3$) as described in [12]. Then the Hamiltonian blocks $[\tilde{\mathbf{H}}_{01}^{(i,i+1)}]_\Phi$ describing the coupling between two adjacent systems i and $(i{+}1)$ (see **Fig.1b**) are approximated as $[\tilde{\mathbf{H}}_{01}^{(i,i+1)}]_\Phi \approx [\mathbf{U}_i]_\Phi^\dagger [\mathbf{H}_{01}^{(i+1)}]_{x\mathbf{K}_{yz}} [\mathbf{U}_{i+1}]_\Phi$, where $[\mathbf{U}_i]_\Phi$ is a unitary matrix whose columns are given by the URBF of the i–th material [12]. Once the blocks of the Hamiltonian matrix in the URBF basis have been determined, the transmission and the $R_{\rm C}$ across the (semi)metal-TMD contacts were calculated according to **Eqs.(1)** and **(2)** in **Fig.1**. We verified that for ballistic transport the $R_{\rm C}$ is, as expected, practically independent of the contact length $L_{\rm C}$ (see **Fig.1a**). The $R_{\rm C}$ values reported in the paper have been obtained for $L_{\rm C}$=10 nm.

III. n–type contacts and link to experiments

For n–type contacts we focused on MoS_2, which is known to favor an n–type behaviour [7], [17], in contact with a

low work function and CMOS compatible metal (Al). For the Al–MoS_2 system, at the minimum energy metal–TMD distance (MED) d=0.27 nm, we observe in **Fig.3a** a large density of MIGS, resulting in FLP, in a distortion of the MoS_2 band structure with respect to the free standing case and in a SBH for electrons of about 0.3 eV. To reduce the Al to MoS_2 orbitals interaction, we interposed an insulating buffer layer consisting of a monolayer hBN and resulting in d=0.71 nm. The Al–hBN–MoS_2 structure exhibits a negligible SBH of ≈9 meV (**Fig.3b**), which is consistent with the Ohmic behaviour experimentally reported for the same system at room temperature [18]. Such a small SBH is also in agreement with the Schottky–Mott rule considering an Al work function WF=4 eV and an MoS_2 electron affinity (χ) of 4.2 eV.

For the Al–MoS_2 and Al–hBN–MoS_2 systems, **Figs.4a** and **4b** report respectively the calculated transmission $T_{k_y}(E)$ and conductance spectrum $G_{k_y}(E)$, that determine R_C through **Eqs.(1)** and **(2)** in **Fig.1**. If we compare the Al–hBN–MoS_2 system (red triangles) with an Al–MoS_2 stack featuring the same d=0.71 nm (black circles), we observe a similar energy dependence of T_{k_y} and G_{k_y}. However in the Al–MoS_2 the T_{k_y} is smaller due to a steeper decay of the wave-functions in the tunnelling region. If we now reduce d to 0.35 nm in the Al–MoS_2 system (blue squares), the $T_{k_y}(E)$ for d=0.35 nm is negligible at the Fermi level due to a SBH of ≈200 meV. Whereas at energies E above the SBH the transmission is much larger than the $T_{k_y}(E)$ calculated for the d=0.71 nm case. Hence, the charge transport in the d=0.35 and d=0.71 nm cases for Al–MoS_2 is limited by the SBH and the TB, respectively, both resulting in a large R_C value above 100 $k\Omega\,\mu$m (**Fig.5**). A better R_C around 3.5 k$\Omega\,\mu$m is calculated for d=0.53 nm, thus resulting in the non–monotonic R_C versus d trend shown in **Fig.5** (red bars). The Al–hBN–MoS_2 system shows an R_C≈3 k$\Omega\,\mu$m (blue bar). These R_C values are still too large for the requirements of CMOS transistors [19].

Very recently it was experimentally shown that the semimetal Bi can provide an essentially Ohmic, n–type contact to MoS_2 [8]. We performed *ab–initio* simulations of the resistance in the Bi–MoS_2 system sketched in **Fig.6a-b**. **Fig.7** reports the projected electronic structure close to the conduction band (CB) minimum for the Bi–MoS_2 VHJ. For the MED, we observe in **Fig.7a** a branch of MIGS that crosses E_F resulting in FLP and in a SBH≈72 meV. The corresponding transport simulations provide an R_C of about 4.5 k$\Omega\,\mu$m, which is much larger than the 123 $\Omega\,\mu$m value experimentally reported in [8]. However, the distance d between Bi and MoS_2 can change in the sub-angstrom range due to the formation of Moiré superstructures or misalignments between the two systems [16], therefore we investigated the influence of small d variations. **Fig.7b** shows that even small alterations of d can sizeably modify the band structure of the VHJ; in fact for d=0.45 nm the branch of MIGS is suppressed and the SBH is essentially zero. **Fig.8a** shows the ballistic R_C (red circles) for different d values. At the MED, the high R_C stems from the SBH≈72 meV, whereas at the largest d value the R_C is dominated by the TB. **Fig.8a** unveils the existence of an optimum distance (d=0.45 nm) that minimizes R_C at 410 $\Omega\,\mu$m (see also **Fig.5**). Since **Fig.8a** suggests that the ballistic resistance of the monolayer MoS_2 is much lower than 410 $\Omega\,\mu$m, hence we infer that R_C is limited by the transmission across the VHJ and may thus be lowered by opening additional tunneling paths. In order to investigate this point for the complex Bi–MoS_2 system at study, we included a phenomenological self–energy describing a single inelastic optical phonon, and then solved the NEGF equations based on the self–consistent Born approximation. The phonon parameters are representative of the dominant optical phonon in MoS_2 (i.e. D_{op}=5.8×10^8 eV/cm and $\hbar\omega$=47 meV [20]), and the approach is similar to [21]. For d=0.45 nm, the electron-phonon (el–ph) interaction reduces R_C to 190 $\Omega\,\mu$m (see **Fig.8a**), that improves the agreement with the experiments in [8]. Indeed **Fig.8b** shows that the el–ph interaction broadens the current spectrum and increases the current, in qualitative agreement with [21].

IV. p–TYPE CONTACTS AND LINK TO EXPERIMENTS

Metals with high WF and TMDs with low χ are good candidates for p–type Ohmic contacts. Therefore, we analyzed WSe_2 (χ≈3.5 eV) in contact with Au (WF≈5.3 eV), namely the system experimentally investigated in [17]. Spin orbit coupling (SOC) is large in heavy $5d$ elements, therefore we introduced SOC in our DFT calculations. **Fig.9b** shows that DFT results reproduce well the experimental ≈0.46 eV splitting of the valence band maximum experimentally reported in [22]. The MED is d=0.28 nm and matches with the STEM measurements for Au evaporated on WSe_2 [17]. For such a d value, DFT simulations predict a large p–type SBH of 0.57 eV due to MIGS (**Fig.9a**), in qualitative agreement with the very low current values experimentally reported in Au to monolayer WSe_2 contacts [17]. **Fig.9b** shows that, similarly to the n–type contacts, by slightly increasing d the SBH is drastically reduced to ≈70 meV. Very interestingly, a similar finding has been reported in experiments: when a metal deposition process relying on a sacrificial selenium buffer layer is used, an increase of the distance d and a decrease of the SBH down to 60 meV have been observed [17]. The reduction of the SBH shown in **Fig.9b** for d>MED suggests an R_C trend similar to the one shown in **Fig.8a** for the Bi–MoS_2 VHJ. Results for the R_C of the Au-WSe_2 VHJ will be presented at the conference.

V. CONCLUSIONS

We used an in–house developed, *ab–initio* transport methodology to investigate metal contacts to monolayer MoS_2 and WSe_2, in particular focusing on the trade–off between SBH and TB. We confirmed by simulations the superior performance of the bismuth–MoS_2 n–type contact. We also showed that the Au–WSe_2 system provides a pathway to an Ohmic p–type contact. The paper conveys both advancements in the simulation methodology, and physical insight for the engineering of metal contacts to TMDs.

Acknowledgement: This work was supported by the Italian MIUR through the PRIN Project 2017SRYEJH, and the French ANR, Tunne2D project (ANR-21-CE24-0030).

References

[1] A.I. Khan *et al.*, *Appl. Phys. Lett.*, vol.116, n.20, 2020.
[2] G. Iannaccone *et al.*, *Nat. Nanotech.*, vol.13, n.3, p.183-193, 2018.
[3] M.C. Lemme *et al.*, *Nat. Commun.*, vol.13, n.1392, 2022.
[4] C. Kim *et al.*, *ACS Nano*, vol.11, n.2, p.1588-1596, 2017.
[5] G.-S. Kim *et al.*, *ACS Nano*, vol.12, n.6, p.6292-6300, 2018.
[6] Y. Guo *et al.*, *ACS Appl. Mater. Interf.*, vol.7, n.46, 2015.
[7] M. Farmanbar *et al.*, *Advanced electronic materials*, vol.2, n.4, 2016.
[8] P.-C. Shen *et al.*, *Nature*, vol.593, n.7858, pp.211-217, 2021.
[9] K. P. O'Brien *et al.*, *IEEE IEDM*, pp.146-149, 2021.
[10] A.-S Chou *et al.*, *IEEE IEDM*, pp.150-153, 2021.
[11] A. Kumar *et al.*, *IEEE IEDM*, pp.154-157, 2021.
[12] M. G. Pala *et al.*, *Phys. Rev. B*, vol.102, p.045410, 2020.
[13] https://github.com/marcopala/Green-Tea-.
[14] P. Giannozzi *et al.*, *J. Phys. Condens. Matter*, vol.29, n.46, 2017.
[15] P. Khakbaz *et al.*, *Solid-State Electronics*, vol.184, p.108039, 2021.
[16] Z. Zhang *et al.*, *ACS Appl. Mater. Interf.*, vol.14, n.9, p.11903, 2022.
[17] G. Kwon *et al.*, *Nature Electronics*, vol.5, n.4, p.241-247, 2022.
[18] X. Cui *et al.*, *Nano Letters*, vol.17, n.8, p.4781-4786, 2017.
[19] https://irds.ieee.org/images/files/pdf/2021/2021IRDS_MM.pdf.
[20] X. Li *et al.*, *Phys. Rev. B*, vol.87, n.11, p.115418, 2013.
[21] Á. Szabó *et al.*, *Nano Letters*, vol.19, n.6, p.3641-3647, 2019.
[22] Y. Zhang *et al.*, *Nano Letters*, vol.16, n.4, p.2485–2491, 2016.

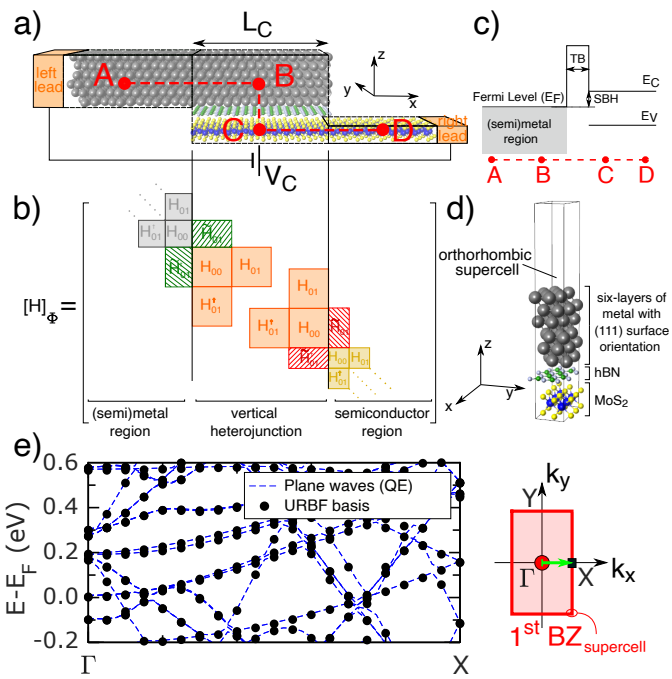

$$G_{k_y}(E) = \frac{2q^2}{h} T_{k_y}(E) \left(-\frac{df_0(E-E_F)}{dE}\right) \quad (1)$$

$$\frac{1}{R_C} = \frac{1}{2\pi} \int_{k_y} \left[\int_{-\infty}^{+\infty} G_{k_y}(E)\, dE\right] dk_y \quad (2)$$

Fig. 1: a) Simulated structures consisting of the (semi)metal region at the left, the MoS_2 region at the right, and the actual (semi)metal–MoS_2 VHJ in the center having a length L_C. b) Sketch of the block tridiagonal Hamiltonian matrix along the (semi)metal–MoS_2 heterostructure, where $[\tilde{\mathbf{H}}_{01}]_\Phi^{i,i+1}$ are the Hamiltonian blocks describing the coupling between two adjacent sub–systems. c) Simplified sketch of the band diagram along the A–B–C–D path depicted in a), showing the Schottky barrier height (SBH) and tunnelling barrier (TB). d) Side view of the orthorhombic Al–hBN–MoS_2 supercell used for transport simulations. e) Electronic structure along the Γ–X path (see the green arrow) for the VHJ shown in d) obtained either with DFT calculations by QE or with the URBF basis of this work. Bottom panel: equations used to calculate R_C. **Eq.(1)** gives the Landauer expression for the conductance spectrum $G_{k_y}(E)$, **Eq.(2)** reports the R_C definition, obtained by integrating $G_{k_y}(E)$ over the Bloch vector k_y. $T_{k_y}(E)$ is the transmission spectrum for a given transverse vector k_y and $f_0(E-E_F)$ is the Fermi–Dirac occupation function with E_F being the Fermi level.

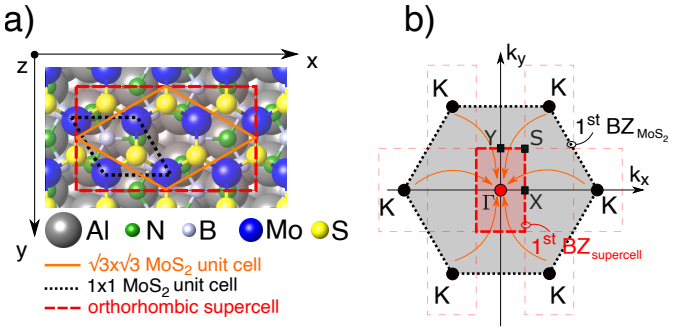

Fig. 2: a) Top view of the orthorhombic supercell used for the simulations of the Al–hBN–MoS_2 VHJ. b) First Brillouin zone (1st BZ) for the primitive MoS_2 unit cell (grey hexagon), and 1st BZ for the orthorhombic supercell (red rectangle). Arrows show that the K, K′ points of the 1st BZ of MoS_2 are backfolded at the Γ point in the 1st BZ of the supercell.

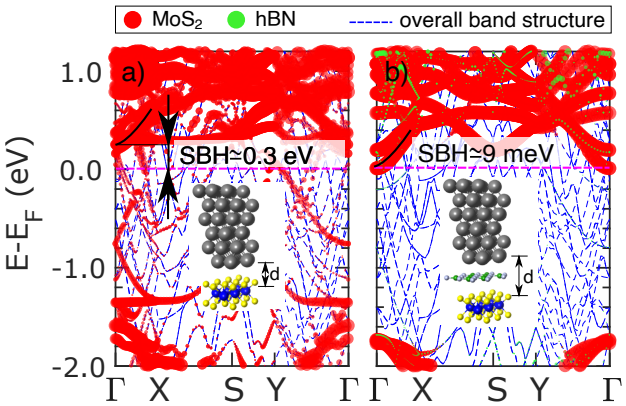

Fig. 3: Projected electronic structure along the high symmetry points shown in **Fig.2b** for: a) the Al–MoS_2 VHJ at the MED d=0.27 nm; b) the Al–hBN–MoS_2 VHJ with a MED d=0.71 nm. The size of red and green circles is proportional to the weight of the projection respectively on MoS_2 and hBN orbitals.

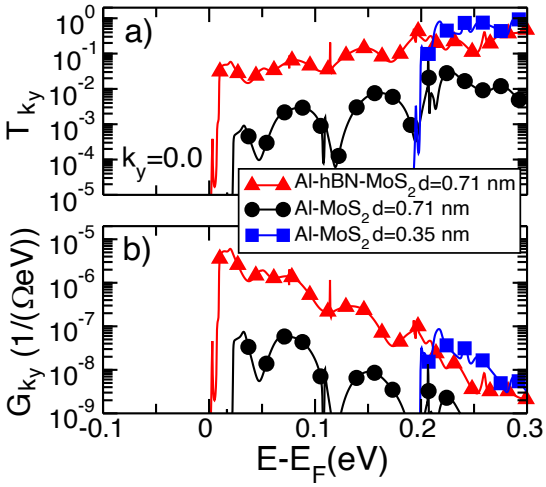

Fig. 4: a) Transmission, T_{k_y}, and b) conductance spectra, G_{k_y}, (see **Eq.(1)** in **Fig.1**) versus the energy for the Al–MoS_2 VHJ with different d values, and for the Al–hBN–MoS_2 system. Results are shown for k_y=0. E_F denotes the Fermi level.

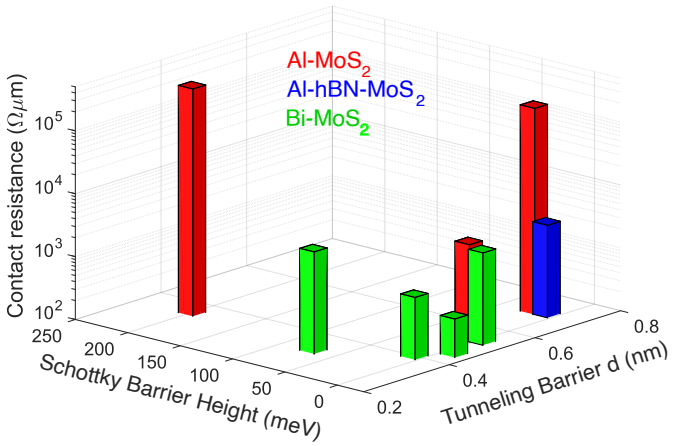

Fig. 5: Numerically calculated R_C for different n–type contacts to MoS_2.

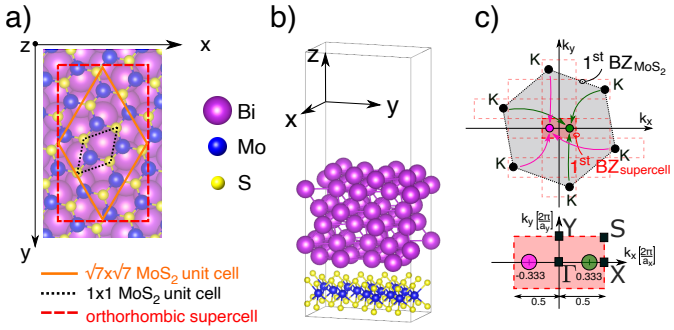

Fig. 6: a-b) VHJ between bismuth (Bi) and MoS_2. c) Brillouin zone (BZ) for the primitive MoS_2 unit cell (grey hexagon), and BZ for the supercell (red rectangle). Arrows show that the K, K′ points of the primitive BZ of MoS_2 are backfolded at points $[\pm 1/3(2\pi/a_x),0]$ in the BZ of the orthorhombic supercell.

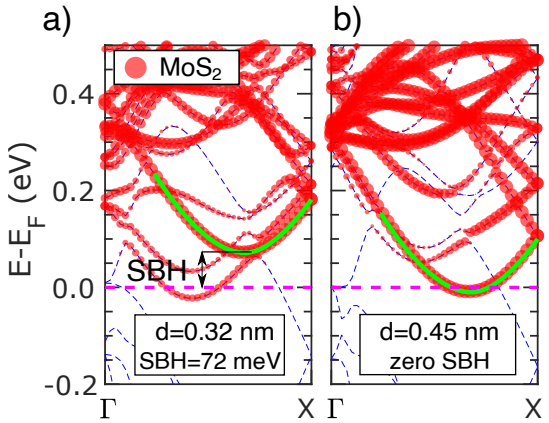

Fig. 7: Electronic band structure projected on MoS_2 for the Bi–MoS_2 VHJ close to the CB minimum. Simulation results are shown for a) the MED (d=0.32 nm) and b) d=0.45 nm. The size of the red circles is proportional to the weight of the projection on MoS_2. The green line identifies the CB branch with the minimum in k_x=0.33 $[2\pi/a_x]$ corresponding to the CB minimum of free–standing MoS_2 (see **Fig.6c**).

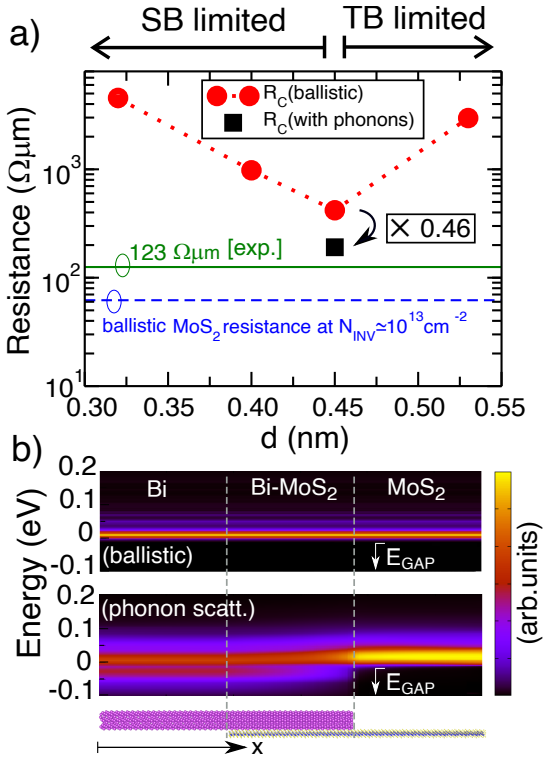

Fig. 8: a) Resistance R_C for the Bi–MoS_2 contact (red circles) versus the Bi–MoS_2 distance d. For d=0.45 nm a decrease of R_C by a factor ∼2 is obtain upon the inclusion of an inelastic el-ph interaction (black square). The ballistic resistance of MoS_2 is also shown for comparison (dashed line) for a charge density corresponding to a free standing MoS_2 with the CB aligned as the green branch of **Fig.7b**. The experimental R_C from [8] is 123 Ω μm (solid line). b) Spatial and energy–resolved current spectrum for ballistic transport (top) and for the inclusion of electron-phonon interaction (bottom).

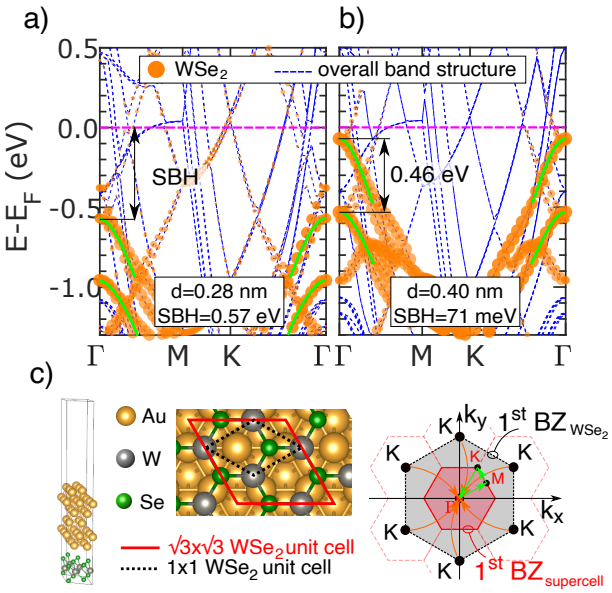

Fig. 9: Electronic band structure projected on WSe_2 along the path shown in c) for the Au–WSe_2 VHJ close to the VB maximum (VBM) and for a) MED (d=0.28 nm) and b) for d=0.40 nm. Green lines are guides for the eyes and identify the spin–splitted VBM. c) Simulated atomic structure with corresponding BZs.